SUPPORTING INFORMATION

Vertically Emitting Indium Phosphide Nanowire Lasers

Wei-Zong Xu[1,2,4†], Fang-Fang Ren[1,2,4†*], Dimitars Jevtics[3], Antonio Hurtado[3*], Li Li[1], Qian Gao[1],

Jiandong Ye[2], Fan Wang[1,5], Benoit Guilhabert[3], Lan Fu[1], Hai Lu[2,4], Rong Zhang[2,4], Hark Hoe Tan[1],

Martin D. Dawson[3], and Chennupati Jagadish[1]

[1]*Department of Electronic Materials Engineering, Research School of Physics and Engineering, The Australian National University, Canberra, Australian Capital Territory 2601, Australia*

[2]*School of Electronic Science and Engineering, Nanjing University, Nanjing 210093, China*

[3]*Institute of Photonics, SUPA Department of Physics, University of Strathclyde, Technology and Innovation Centre, 99 George Street, G1 1RD Glasgow, United Kingdom*

[4]*Collaborative Innovation Center of Advanced Microstructures, Nanjing University, Nanjing 210093, China*

[5]*Institute for Biomedical Materials and Devices (IBMD), Faculty of Science, University of Technology Sydney, Sydney, New South Wales 2007, Australia*

[†]These authors contributed equally to this work. [*]e-mail: ffren@nju.edu.cn; antonio.hurtado@strath.ac.uk

I. Design of the InP nanowires (NWs) and cat's eye (CE) antennas
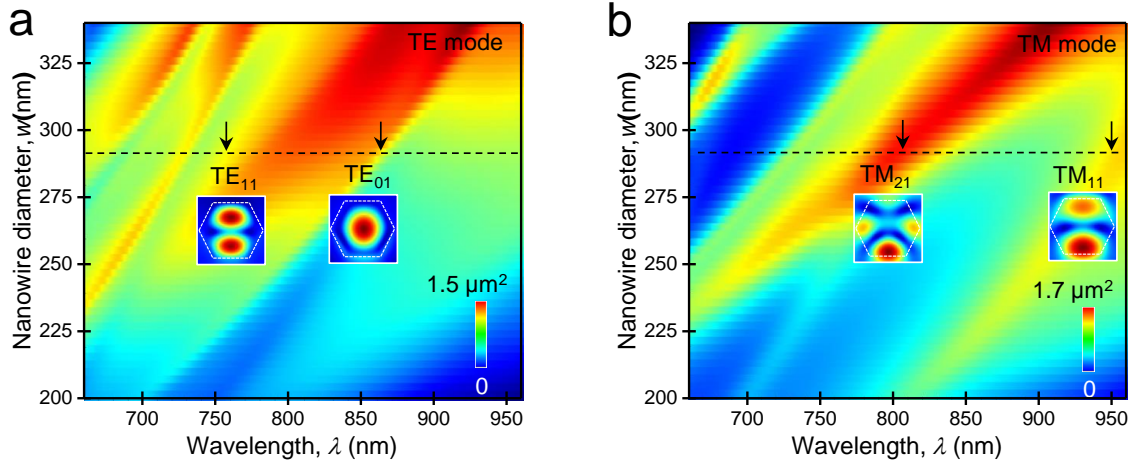
a. Design of the InP NWs

Figure S1. (a,b) Three-dimensionally calculated cross section scattering for the TE modes (i.e. excitation with light polarized along E_x) and TM modes (i.e. excitation with light polarized along E_y) of an InP nanowire (NW) lying horizontally on a quartz substrate as a function of wavelength and NW diameter. The length of the NW is 900 nm. The insets in panel (a) show respectively the configuration of the magnetic field intensities for the TE_{01} and TE_{11} modes when the diameter of the NW is set equal to 290 nm. The insets in panel (b) show respectively the configurations of the electric field intensities for the TM_{11} and TM_{21} modes when the diameter of the NW is also set equal to 290 nm. Under excitation with light polarized along E_x, the spectral positions for the TE_{01} and TE_{11} modes are located around 750 and 870 nm, respectively, close to the photoluminescence (PL) spectral peaks for InP NW at cryogenic (~7 K) and room temperatures (RT), respectively. These modes result in an enhanced field confinement in the InP NW, increasing the radiative recombination rate and thus leading to a higher internal quantum efficiency (IQE).

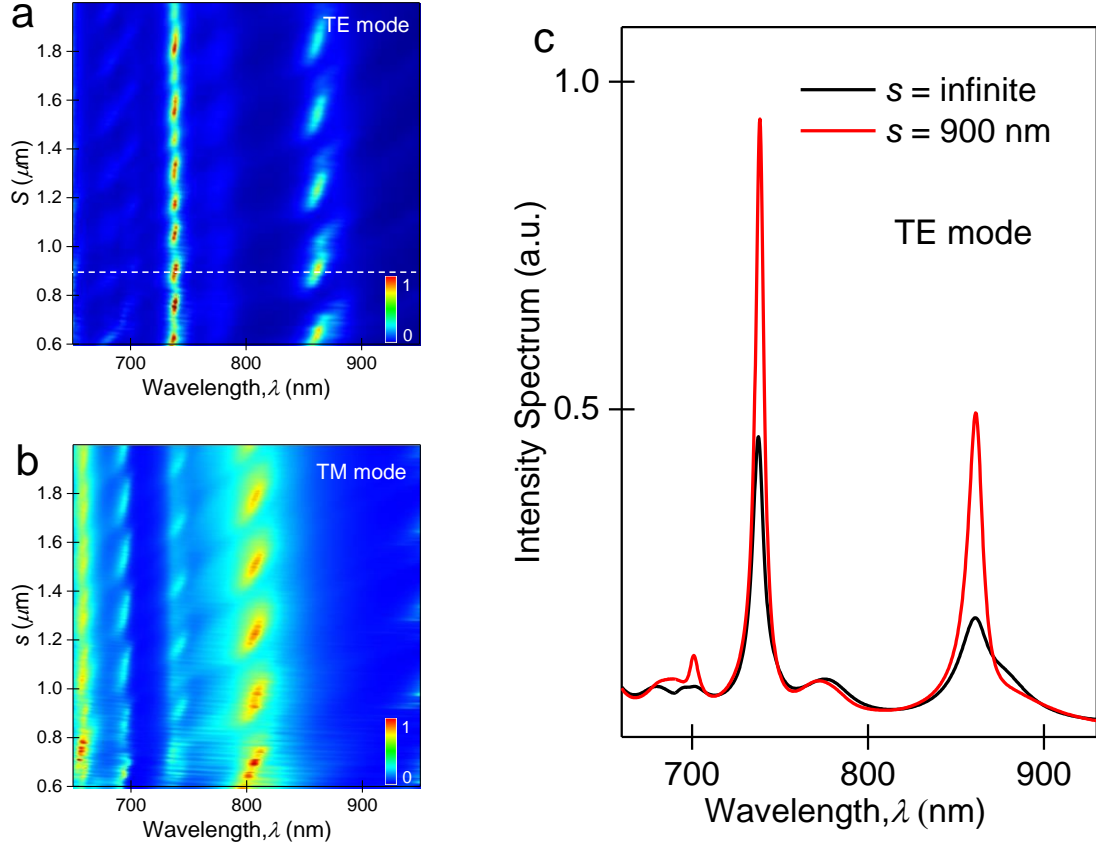**b. Optimization of CE antennas to form a high *Q*-factor cavity**

Figure S2. (a,b) Normalized intensity spectra of the electric/magnetic fields in the InP NW (diameter *w* = 290 nm and length *L* = 900 nm) under excitation with light polarized along E_x or E_y as a function of the parameter *s*. The latter, indicating the distance of the inner circular grating from the center of the CE antenna, is varied from 600 nm to 2 μm. Plots (a) and (b) are used to optimize the value of *s* in the design of the CE antenna for Sample A. Under E_x incidence, a series of maxima in intensity are observed due to Fabry-Perot resonances for values of *s* ≈ 650, 900, 1200, 1500 nm, etc., at the wavelength of λ = 870 nm. Similar characteristics could also be observed under excitation with light polarized along E_y. To ensure minimal damage from the focused ion beam during the fabrication process, an optimal value of *s* = 900 nm is finally chosen for the design of the CE antennas of this work. (c) Intensity spectra of the electrical field in the NW (*w* = 290 nm and *L* = 900 nm) under excitation with light polarized along E_x as a function of wavelength when the value of *s* is set to either 900 nm or an infinite value. At a wavelength λ = 870 nm, the cavity *Q*-factor is calculated to be ~ 32.4 when *s* is set with an infinite value, and

increases to ~ 89.9 when s = 900 nm. Around the wavelength, λ of 750 nm, the cavity Q-factor is calculated to be ~ 99.6 when s is set with an infinite value, and increases to ~ 131.8 when s = 900 nm. Hence, integrating the inner circular grating permits the achievement of a higher Q-factor cavity with strong field confinement.

c. Design of the CE antennas for excitation of surface plasmons

The structural parameters of the CE antenna, including grating period (p), metallic concentric grating width (b) and depth (d), inner circular grating distance (s), and split-gap width (g), are optimized using FDTD methods in order to enable the excitation of surface plasmon (SP) waves on the surface of Al grating at the emission wavelength of the InP NWs (λ = 870 nm).

Based on Helmholtz reciprocity theorem [S1], the SP excitation occurs at the interface of the Al antenna and the dielectric SiO$_2$ with the assistance of Bragg grating. The period, p, of the Al concentric grating, which is dominant in determining the SP wavelength, can be roughly given by the momentum conservation law:

$$k_{\mathrm{SP}} = k \sin\theta + mG \tag{1}$$

Here, m is an integer, θ is incident angle, and $G = 2\pi / p$ is the reciprocal vector of the periodic grating to compensate for the mismatch in the wave vector between the in-plane momentum $k\sin\theta$ of impinging photons and the SP propagation constant $k_{\mathrm{SP}} = 2\pi\sqrt{\varepsilon_{\mathrm{Al}}\varepsilon_{\mathrm{SiO_2}} / (\varepsilon_{\mathrm{Al}} + \varepsilon_{\mathrm{SiO_2}})} / \lambda$. The parameters $\varepsilon_{\mathrm{Al}}$ and $\varepsilon_{\mathrm{SiO_2}}$ represent the frequency dependent dielectric constants of metal and SiO$_2$, respectively. In the case of the 1st grating order and normal incidence (θ = 0 and m = 1), the grating period, p, can be estimated to be 650 nm. The other parameters, including b, s and g also have influence on the SP excitation, and have been optimized in our work to ensure a maximum reflection by the Al antenna. The grating depth d =300 nm was not optimized here, because it is mainly dependent on the actual diameter of the nanowire used during fabrication.

d. Design of the CE antennas for light-focusing functionality

As mentioned in the manuscript, the periodical circular grating also functions as a lens, focusing the emission at a frequency range that coincides with the one in which beaming of light appears [S2]. The detailed description of how each parameter in a metal antenna affects its far-field distribution can be found as follows.

In Figure S3e, we plot the *E*-field intensity profile (arbitrary units) along the propagating direction on *x-z* planes for Sample A with the following parameters: grating period, p = 650 nm, metallic concentric grating width b = 200 nm and depth d = 300 nm, split-gap width g = 200 nm, and inner circular grating distance, s = 900 nm, at the resonant wavelength of 870 nm. As indicated in [S3], such an intensity distribution can clearly resolve far-field features. During the simulation, we included a linear profile monitor along the z direction (i.e. the dotted gray line shown in Figures S3a and S3e). This allowed us to examine the *E*-field cross-sectional profile cut along the line x=0. The appearance of a very strong focus can be observed at around z =1 μm (i.e. the point F shown in Figure S3f). For various wavelengths, the beaming effect may also work (see Figure S3g), but for the wavelength at SP mode beaming is maximum [S4]. In other words, the intensity at the focal point (i.e. point F in Figure S3f) of the lens can be enhanced, because the plasmonic lens can generate a beam with reduced diffraction [S4]. Figures S3h-k show how the parameters of the antenna, including p, b, s and g affect on the beaming effect of the emission at the wavelength of 870 nm. The individual effect of these parameters can be summarized as follows:

(i) grating period p. As shown in Figure S3h, we swept the values of p with fixed parameters b = 200 nm, d = 300 nm, s = 900 nm and g =200 nm. When the value of p = 650 nm, the E intensity at the focal point is maximum due to the SP excitation.

(ii) grating width b, inner circular grating distance s, and split-gap width g. As for the effect of parameters b, s and g on the beaming, we can refer to the simulation results shown in Figures S3i-k. The paramerters of b =200 nm, s = 900nm and g =200nm are finally chosen for the nanowire with a diameter

of 290 nm and a length of 900nm by considering SP excitation, maximum E intensity at the focal point, minimal footprint of the device, as well as the feasibility in fabrication. It should be mentioned that, during the simulation for Figure S3i, we swept the values of b by fixing parameters p =650 nm, d =300 nm, s = 900nm and g =200nm. For Figure S3j, we swept the values of s by fixing parameters p =650 nm, d =300 nm, b = 200nm and g =200nm. For Figure S3k, we swept the values of g by fixing parameters p =650 nm, d =300 nm, b = 200nm and s =900 nm.
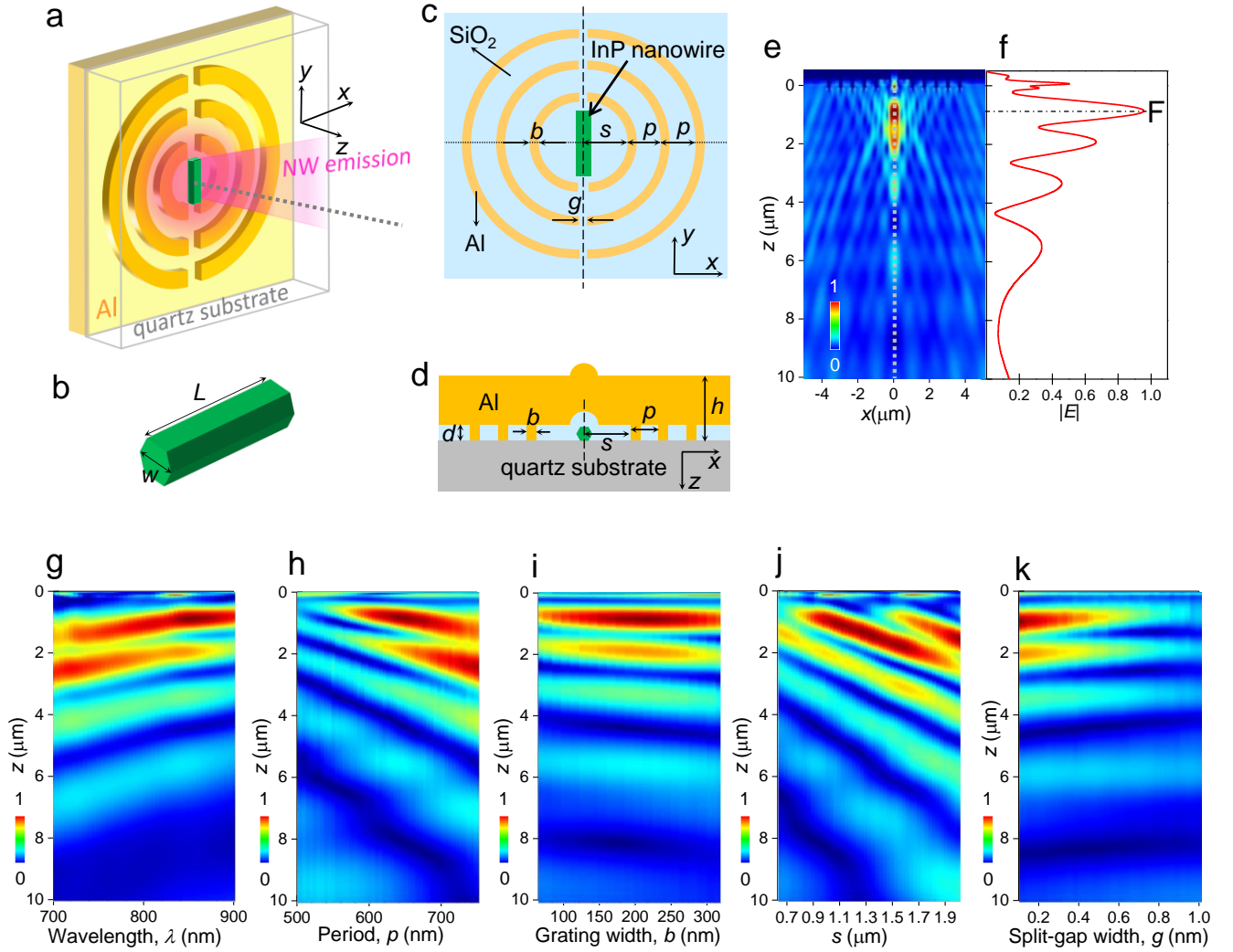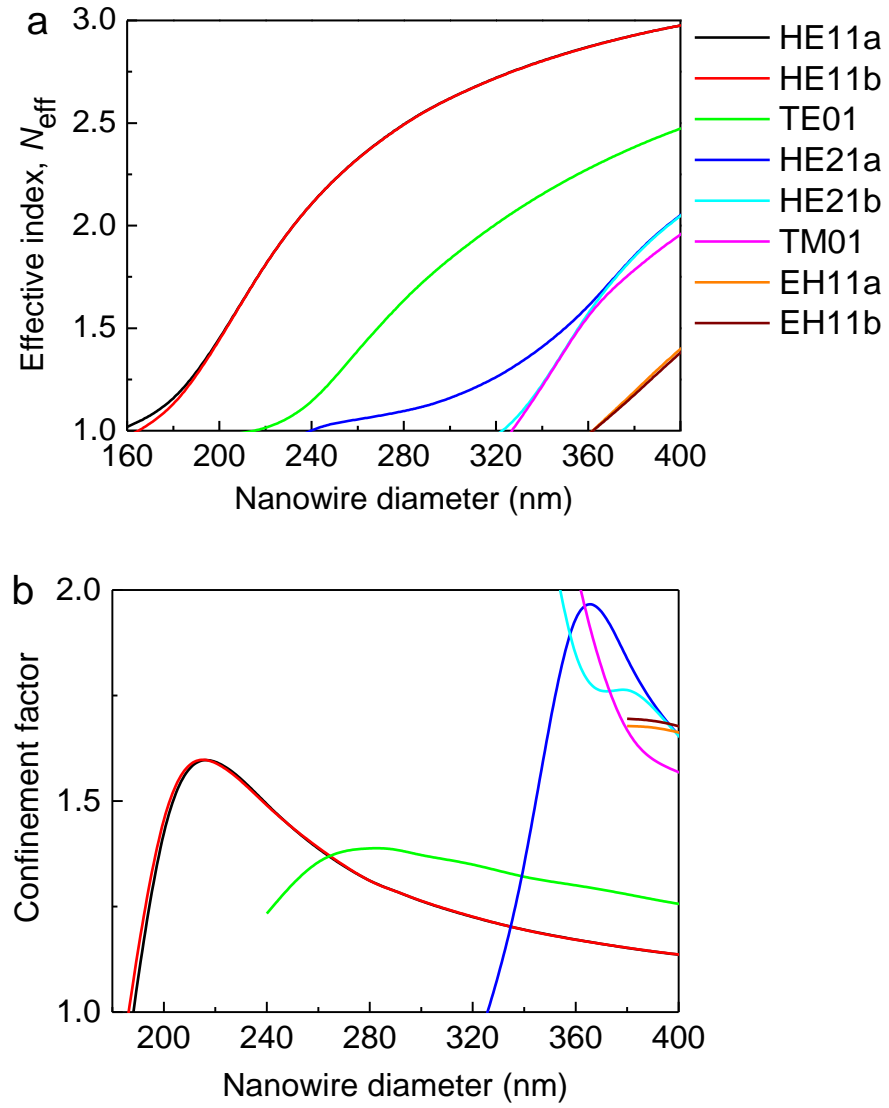

Figure S3. (a) Device layout of the antenna-coupled nanowire laser structure consisting of an InP nanowire embedded in a cat's eye antenna. (b) InP nanowire geometry. (c,d) Top-view & cross-section schematics. (e) Electric field profile along the propagating direction on x-z planes for Sample A. Grating period, p = 650 nm, metallic concentric grating width b = 200 nm & depth d = 300 nm, split-gap width g

= 200 nm, and inner circular grating distance, s = 900 nm (at the resonant wavelength of 870 nm). (f) Electric field profile along the line x=0 shown in e. (g-k) Electric field profile along the line x=0 for various antenna parameters, p, b, s and g. Colour bar shows normalized intensity ($|E|$) (dark blue = 0, red = 1).
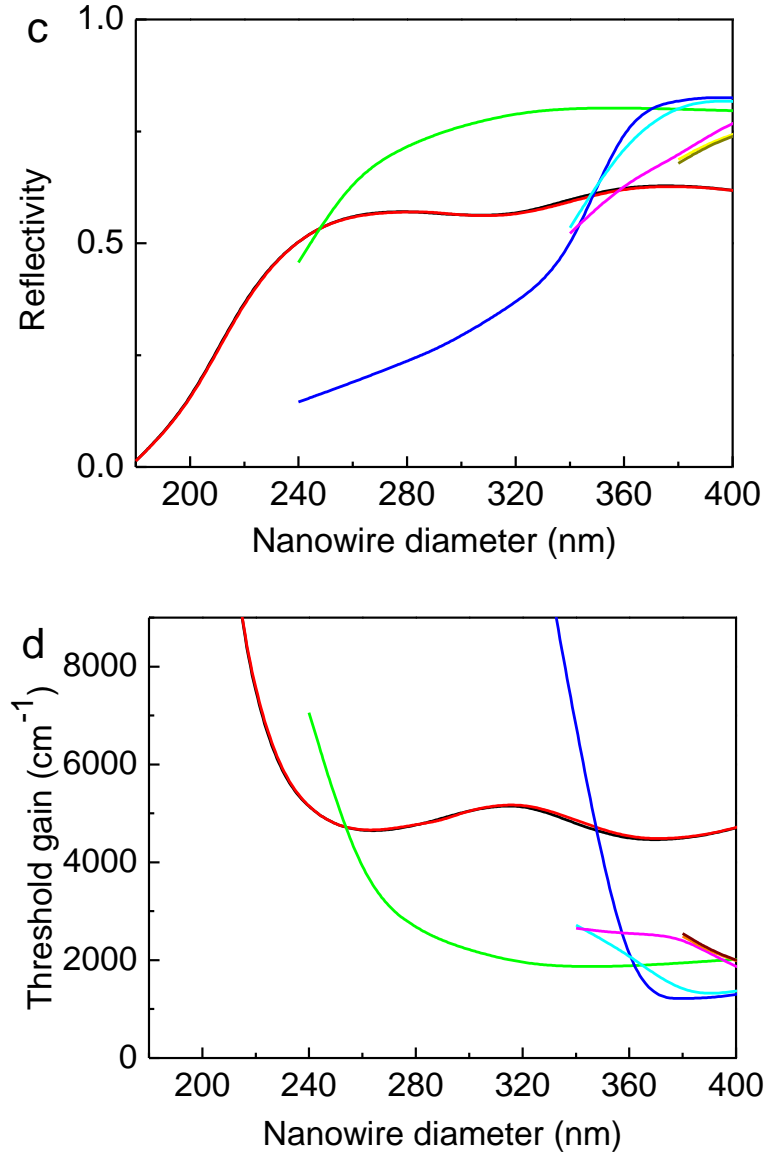
II. Threshold gain modeling

Figure S4. (a,b) Effective refractive index and confinement factor versus the NW diameter for the modes supported by an InP NW horizontally lying on a quartz substrate at the wavelength of 870 nm. (c) Reflectivity of the supported modes at the NW end facets (NW/air interface). (d) Threshold gain for the supported modes as a function of NW diameter calculated using data from (a-c).

The threshold condition for lasing in a semiconducting NW is achieved when the round-trip gain for a guided mode in the NW equals the round-trip losses. In a NW, the optical losses are dominated by mirror losses occurring at the two end facets of the NW. As a result, the threshold condition can be estimated by:

$$\Gamma g_{\mathrm{th}} \approx \frac{1}{L}\ln\frac{1}{R} \tag{2}$$

where Γ is the mode confinement factor, g_{th} is the threshold material gain, L is the NW length, and R is the mode reflectivity at both facets of the NW. The confinement factor for each supported mode can be obtained from the optical mode profiles. For a dielectric waveguide this can be calculated using the following expression:

$$\Gamma = \frac{c\varepsilon_0 n_a(\omega)\iint_{\mathrm{active}}\frac{1}{2}|\mathbf{E}|^2\, dxdz}{\iint\frac{1}{2}\mathrm{Re}|\mathbf{E}\times\mathbf{H}^*|\cdot\hat{z}\, dxdz} \tag{3}$$

where $\mathbf{E}$ and $\mathbf{H}$ are respectively the complex electric and magnetic fields of the waveguide modes, c is the light speed in vacuum, ε_0 is the vacuum permittivity, and n_a is the refractive index of the gain medium (InP) at the frequency ω of the guided mode. The integral area in the numerator is defined as the NW cross-section in the xz plane, and the integral part in the denominator is taken across the entire simulation cross-section area. It is found that Γ is larger than 1 for all modes, as shown in Figure S4b. This feature arises from the strong guiding behavior of semiconducting NWs, which finally results in a slower group velocity and consequently large modal gain.
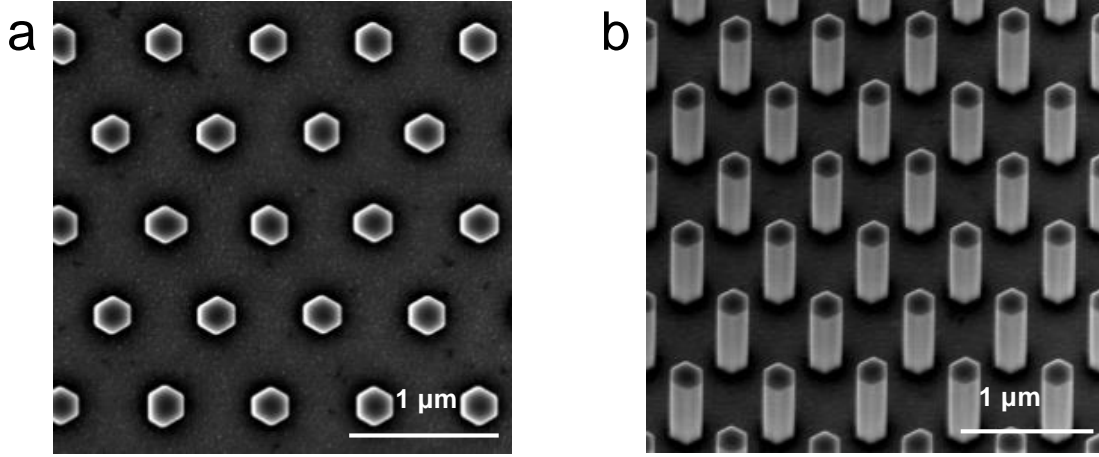
III. Growth of InP nanowires (NWs)

Figure S5. Scanning electron microscopy (SEM) images of wurtzite (WZ) phase InP NWs grown by selective-area MOVPE (SA-MOVPE) (a) Top view. (b) 30˚ tilt view. To grow the NWs, a 30-nm thick SiO_2 layer was first deposited on a (111)A InP substrate as a mask. Then, electron beam lithography (EBL) was used to produce a pattern formed by circles arranged in a hexagonal array. Chemical etching of the SiO_2 layer through this pattern resulted in the formation of an array of holes (openings) for the NWs to grow. Afterwards, the patterned substrate was placed in a horizontal flow low-pressure MOVPE system, using trimethylindium (TMIn) and phosphine (PH_3) as the precursors for InP NW growth. The resultant NW arrays exhibit excellent uniformity in size and spatial distribution as can be seen from plots (a) and (b). An average NW diameter, w, of 290 nm was obtained. Finally, the NWs were transferred from the substrate onto a quartz substrate where the average NW length, L, was measured to be equal to 900 nm.

IV. Hybrid fabrication of room temperature (RT) InP NW CE lasers by using nano-TP technique
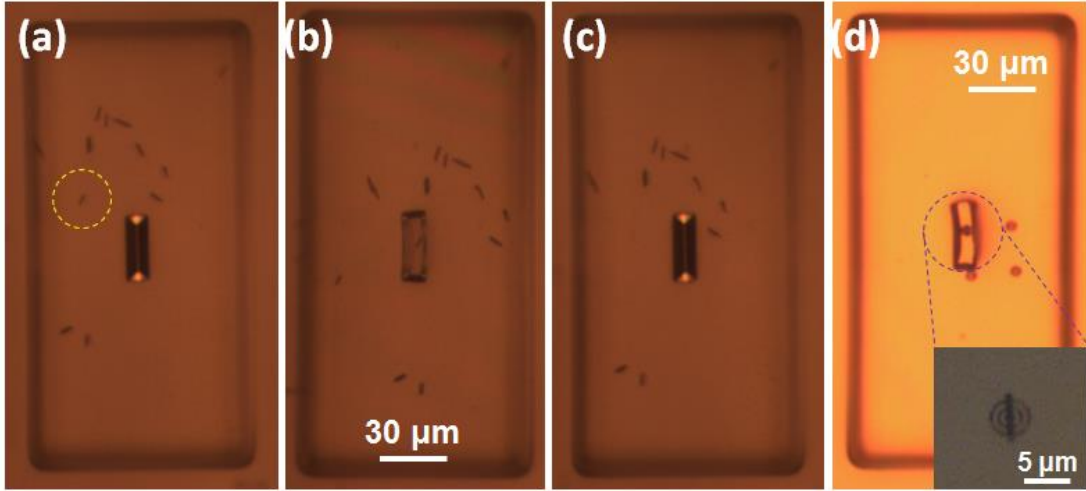

Figure S6. Sequential images captured with an optical system incorporated in the nano-TP toolkit illustrating the processes for the fabrication of hybrid InP NW CE lasers. (a) The polymer (PDMS) μ-stamp is aligned with an individually selected InP NW lying down on a donor *Si* substrate, marked with a dashed yellow circle. (b) Surface contact between μ-stamp and NW is produced to capture the NW. (c) The NW has been captured from the donor substrate and by the μ-stamp for its transfer to the receiving surface. (d) The μ-stamp is aligned with the central gap of the CE antenna, where surface contact is produced for NW release at the desired location. The inset at the bottom shows an image of the hybrid device with the InP NW laser positioned at the central gap of the CE nanoantenna.

The threshold gain for lasing in the NW with ultra-small geometric volume is very high, especially at room temperature (RT). Consequently, RT lasing was not observed from the InP NW CE lasers when the NWs dimensions are 290 nm in diameter and 900 nm in length. However, lasing was successfully achieved at low temperature (7 K) (see results from Sample A in the main manuscript). To demonstrate RT lasing from this type of InP NW CE lasers, a nanoscale Transfer-Printing (nano-TP) technique was used to integrate an InP NW of larger dimensions (435 nm diameter and 5 μm length) with a pre-fabricated CE antenna. The latter was fabricated on *Al* on a quartz substrate with standard e-beam evaporation for the metal layer and FIB etching for the patterning of the antenna design. The nano-TP

technique relies on the adhesive properties of bespoke PDMS elastomeric μ-stamps to 'pick up' and 'release' individually selected NWs, thus allowing their transfer from their original substrate to targeted locations onto diverse or patterned surfaces. Prior to carry out the nano-TP experiments, the vertically-aligned NWs (see for example Figure S5b) were removed from their growth substrate and transferred to a donor substrate (*Si*) where they lay horizontally. Then, the nano-TP technique was used to controllably pick up a single InP NW from the donor *Si* substrate and subsequently print it in the central gap of the fabricated CE antenna. Figure S6b shows the NW as it is being captured with the μ-stamp, with its tip deforming as surface contact is produced between μ-stamp and NW. Figure S6c shows now that the NW had been lifted-off from the surface and picked up by the μ-stamp. After this, the μ-stamp (with the captured NW) was moved to the receiving surface and aligned with the desired printing position. There, surface contact between the μ-stamp and receiving surface was produced to release the NW at the central gap of the CE antenna. Full details on the nano-TP technique can be found in refs [S5,S6]. With this fabricated hybrid InP NW CE structure (as fully detailed in the main manuscript) RT lasing with reduced threshold was achieved at the wavelength of ~ 870 nm.

V. RT radiation patterns of InP NW CE lasers (supplementary information to Figure 2)
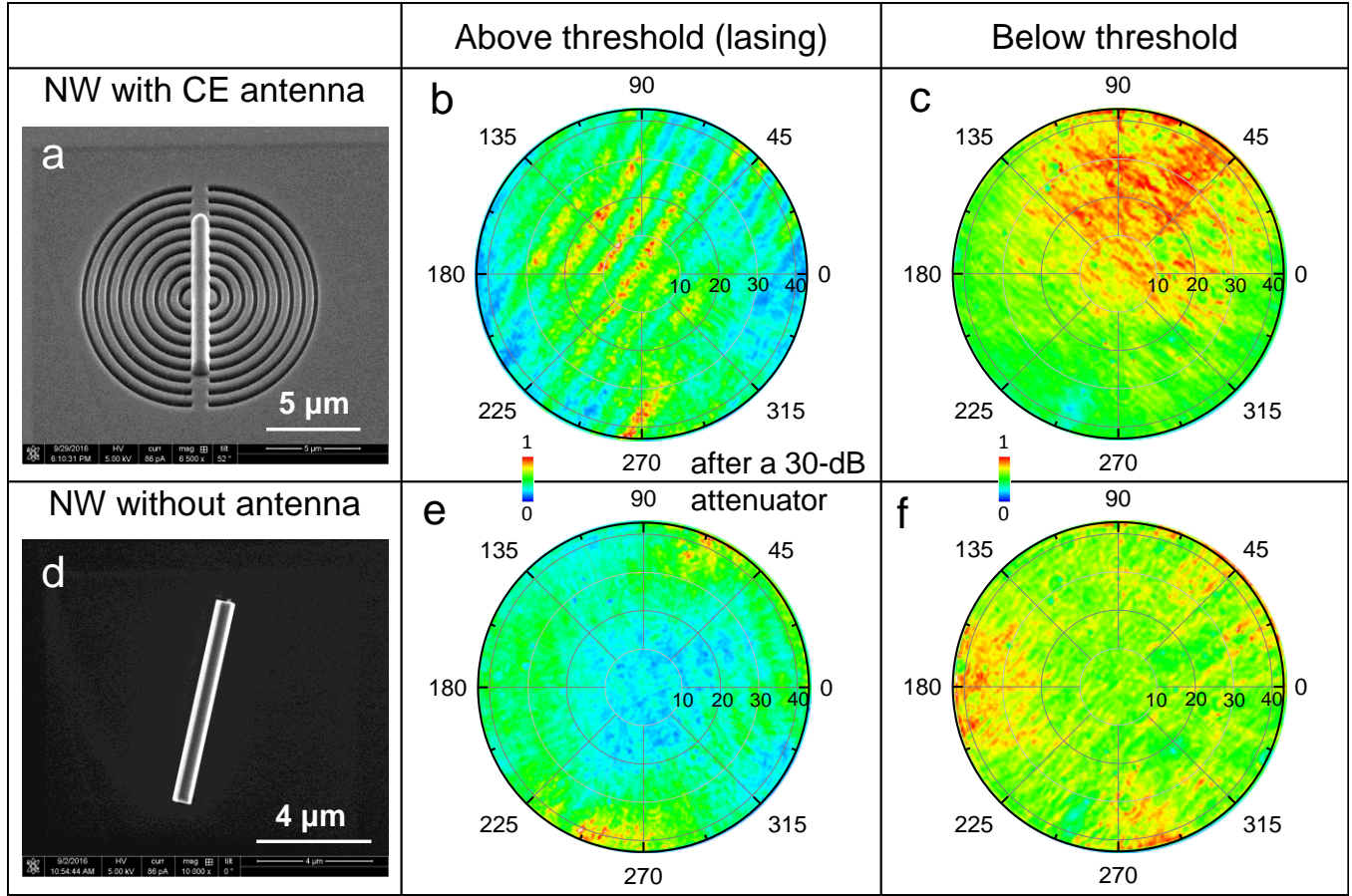

Figure S7. Experimentally measured RT far-field emission patterns of an InP NW CE laser (top) and a bare InP NW laser (bottom) above and below their lasing threshold. The NW dimensions were equal to $w = 600$ nm and $L = 7.5$ μm in both cases. The InP NW CE laser was fabricated using the *in-situ* fabrication procedure described in the Experimental Section of the main manuscript. The structural parameters of the CE nanoantenna were chosen equal to: $p = 650$ nm, $b = 200$ nm, $d = 600$ nm, $g = 700$ nm and $s = 800$ nm. (a) SEM image of the fabricated InP NW CE laser before *Al* deposition. (b,c) Far-field intensity patterns of the InP NW CE laser above and below threshold. (d) SEM image of the bare InP NW laser on *Al* substrate. (e,f) Far-field intensity patterns of the bare InP NW laser above and below lasing threshold. The optical pumping fluences were equal to 12.8 and 0.77 mJ/cm^2, respectively, for the cases where the devices were operated above and below their lasing threshold. It should be noted that the far-field patterns obtained when both devices were above their lasing threshold (panels (b) and (e)) were captured after a 30-dB optical attenuator.

The ultra-small dimensions of the InP NWs in Samples A-C (diameter $w = 290$ nm, length $L = 900$ nm) result in high threshold gain values. This aspect renders the observation of lasing from a bare InP NW of these dimensions (Sample B) extremely challenging, even at low temperatures (~ 7 K), making the measurement of their far-field lasing emission patterns unpractical. Alternatively, we have performed the investigation of the lasing radiation patterns using InP NWs with larger dimensions ($w = 600$ nm, $L = 7.5$ μm) at room temperature. Under those conditions lasing emission was indeed obtained from InP NW devices with and without an integrated CE nanoantenna.

Figure S7 shows first that above the lasing threshold, interference patterns appear in the far-field intensity distribution of both InP NW laser structures with and without the integrated CE nanoantenna. This is a direct result of the spatially coherent emission from the end-facets of the NWs in both devices. Furthermore, the comparison of the far field patterns for both NW devices reveals that the InP NW CE laser exhibits a much improved vertical emission directionality and a higher emission intensity than the bare InP NW laser both above and below the lasing threshold. Hence, these results clearly confirm the strong effect of the integrated CE nanoantenna in enhancing the performance of NW lasers by effectively tailoring the propagating direction of their emitted coherent light.

In addition, the electric field intensities for a bare nanowire (Sample B) and an antenna-coupled nanowire (Sample A) are shown in Figure 2c to investigate their far-field emission characteristics. The corresponding far-field angular distribution profiles of the electric field intensity have been calculated and are shown in Figure S8. A better far-field directionality can be seen from the antenna-coupled nanowire; hence confirming that the cat's eye structure acts as a near-field focusing lens concentrating more the light emission in the vertical direction.
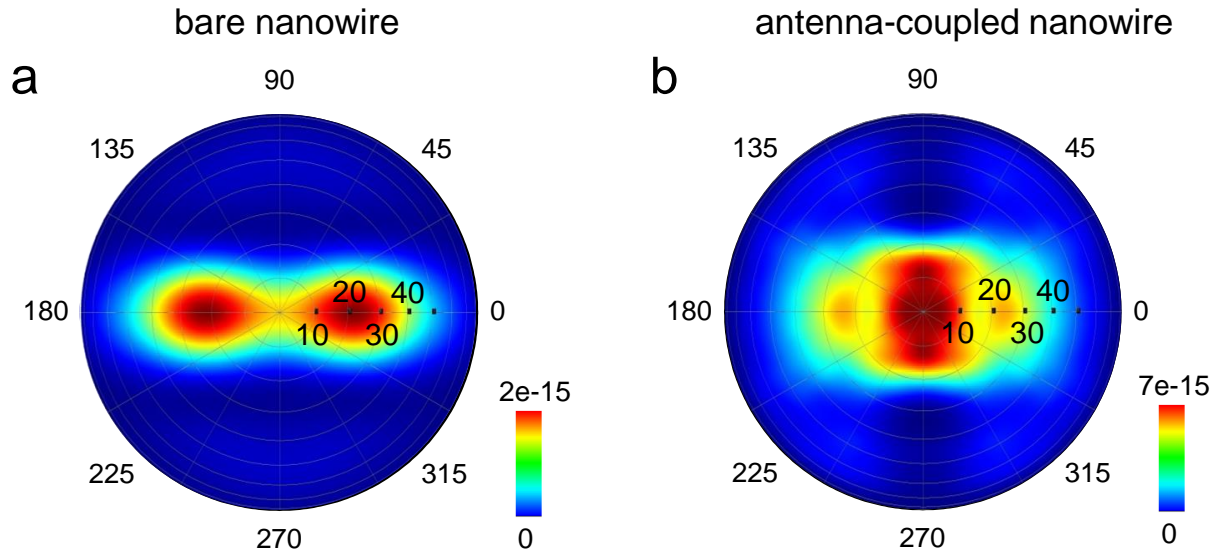
Figure S8. Simulated light angular distribution profiles of (a) a bare nanowire (i.e. Sample B) and (b) an antenna-coupled nanowire (i.e. Sample A) used to investigate their far-field emission characteristics. The colour bar shows intensity ($|E|^2$) normalized to the source used in simulation.

VI. RT lasing of InP NW CE lasers (supplementary experiments to Figure 4)

To better investigate the lasing emission from InP NW-CE nanoantenna lasers, we have compared their emission properties with those of a bare InP NW on a planar *Al* surface. We employed a new hybrid nanoscale Transfer Printing (nano-TP) fabrication technique [S5,S6] to integrate larger-sized InP NWs (w = 435 nm, L = 4.3 μm) onto pre-fabricated *Al* CE nanoantennas (as described in Section IV). This permitted us to fabricate hybrid InP NW CE lasers like that shown in Figure S9a (Sample F). As discussed in Section IV, the achievement of RT lasing requires the use of larger NWs exhibiting lower lasing thresholds. The inset in Supplementary Figure S9a shows an SEM image of the InP NW CE laser (Sample F) fabricated by heterogeneously integrating an InP NW (w = 435 nm, L = 4.3 μm) using nano-TP onto a CE nanoantenna with the following structural parameters: p = 900 nm, b = 650 nm, d = 200 nm, g = 700 nm and s = 600 nm. We also characterized RT light emission from this hybrid InP NW CE laser using the micro-PL setup described in [S5,S6] where optical pumping was carried out with a (λ = 532 nm) pulsed laser (0.75 ns long pulses at 7.2 kHz repetition rate). Supplementary Figure S9a plots the threshold curve of Sample F, showing the onset of RT lasing at a low pumping fluence of ~ 8 mJ/cm^2. Supplementary Figure S9b shows the achievement of narrow spectral emission at RT when the laser is pumped with a fluence of 39 mJ/cm^2. The inset in Figure S9b shows a micrograph of the lasing emission from Sample F at that fluence.

Moreover, to clearly demonstrate the contribution of the CE nanoantenna, we have also fabricated for comparison purposes Sample G, formed simply by a bare InP NW laser (w = 435 nm, L = 4.2 μm) placed on a planar *Al* substrate. Figure S9c shows the RT threshold curve of Sample G revealing a higher lasing threshold (~ 18 mJ/cm^2), while Figure S9d shows its lasing spectrum and a micrograph of the NW laser at a fluence of 62 mJ/cm^2. The higher lasing threshold for Sample G under similar pumping conditions clearly demonstrates the contribution of the integrated CE nanoantenna in reducing the lasing threshold for the InP NW laser.
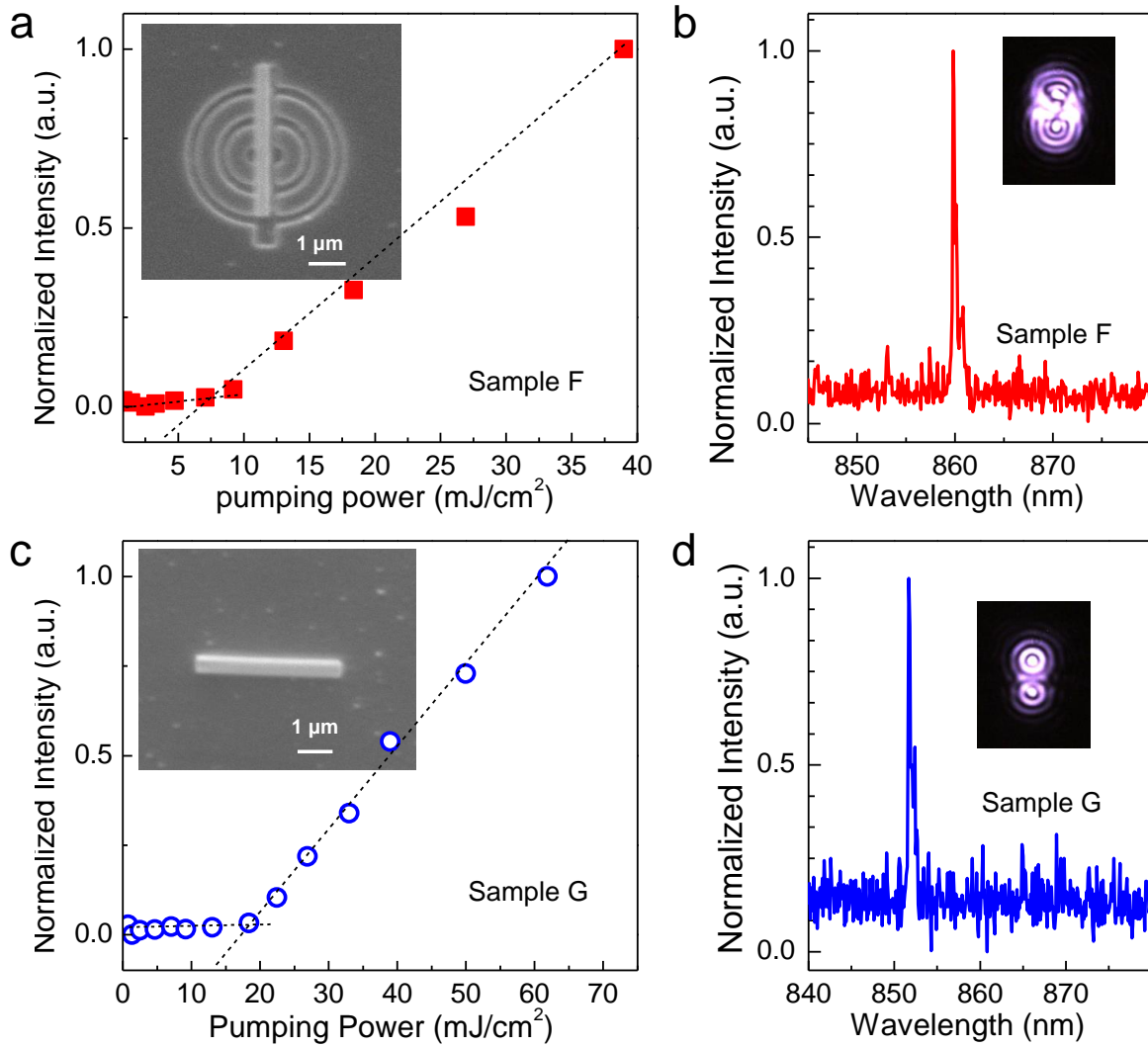
Figure S9. Room temperature lasing characterization of Samples F and G. (a) Lasing threshold curve for the Sample F, showing a lasing threshold of ~ 8 mJ/cm^2. The inset shows the SEM image of Sample F with a single InP nanowire laser (w = 435 nm and L = 4.3 μm) printed onto a CE antenna. (b) Spectral emission of Sample F obtained at the fluence of 39 mJ/cm^2. The inset shows an optical micrograph of the nanowire laser. (c) Threshold curve of the bare nanowire laser (Sample G) with a threshold of ~18 mJ/cm^2. The inset shows the SEM image of Sample G with a single InP nanowire laser (w = 435 nm and L = 4.2 μm) printed onto top of a planar *Al* surface. (d) Emission spectrum of Sample G at a fluence of 62 mJ/cm^2. The inset shows the optical micrograph of the laser at the same pump intensity.

References

[S1] Hutley, M. C. Diffraction Grating; New York: Academic, 1982.

[S2] Garcá-Vidal, F. J. *et al*. Focusing light with a single subwavelength aperture flanked by surface corrugations, *Appl. Phys. Lett.* **83**, 4500 (2003).

[S3] Verslegers L., *et al*. Planar lenses based on nanoscale slit arrays in a metallic film, *Nano Lett.* **9**, 235-238 (2009).

[S4] Yanai, A. *et al*. Plasmonic focusing with a coaxial structure illuminated by radially polarized light, *Opt. Express* **17**, 924 (2009).

[S5] Guilhabert, B. *et al*. Transfer printing of semiconductor nanowires with lasing emission for controllable nanophotonic device fabrication. *ACS Nano* **10**, 3951-3958 (2016).

[S6] Jevtics, D. *et al*. Integration of semiconductor nanowire lasers with polymeric waveguide devices on a mechanically flexible substrate. *Nano Lett.* **17**, 5990-5994 (2017).